Changes in non-dipolar field structure over the Plio-Pleistocene: New paleointensity results from Hawai'i compared to global datasets

Brendan Cych[a,e], Lisa Tauxe[a], Geoffrey Cromwell[b,f], John Sinton[c], and Anthony A.P. Koppers[d]

[a]University of California, San Diego, CA, USA; [b]Occidental College, Los Angeles, CA, USA; [c]University of Hawai'i at Manōa, HI, USA; [d]Oregon State University, Corvallis, OR, USA; [e]Now at University of Liverpool, England, UK; [f]Now at US Geological Survey, California Water Science Center, Santa Maria, CA, USA

This manuscript was compiled on December 1, 2022

A foundational assumption in paleomagnetism is that the Earth's magnetic field behaves as a geocentric axial dipole (GAD) when averaged over sufficient timescales. Compilations of directional data averaged over the past 5 Ma yield a distribution largely compatible with GAD, but the distribution of paleointensity data over this timescale is incompatible. Reasons for the failure of GAD include: 1) Arbitrary "selection criteria" to eliminate "unreliable" data vary between studies, so the paleointensity database may include biased results. 2) The age distribution of existing paleointensity data varies from latitude to latitude so different latitudinal averages likely represent different time periods. 3) The time-averaged field could be truly non-dipolar. Here, we present a consistent methodology for analyzing paleointensity results and comparing time-averaged paleointensities from different studies. We apply it to data from Plio/Pleistocene Hawai'ian igneous rocks, sampled from fine-grained, quickly cooled material (lava flow tops, dike margins and scoria cones) and subjected to the IZZI-Thellier technique; the data were analyzed using the BiCEP method of Cych et al (2021, doi:10.1029/2021GC009755), which produces accurate paleointensity estimates without arbitrarily excluding specimens from the analysis. We constructed a paleointensity curve for Hawai'i over the Plio/Pleistocene using the method of Livermore et al (2018, doi:10.1093/gji/ggy383), which accounts for age distribution and has robust uncertainties. We demonstrate that even with the large uncertainties associated with obtaining a mean field from temporally sparse data, our average paleointensities obtained from Hawai'i and Antarctica (from Asefaw et al., 2021, doi:10.1029/2020JB020834, reanalyzed here) are not GAD-like after about 1.5 Ma.

Paleointensity | Time-averaged geomagnetic field | Geocentric Axial Dipole Hypothesis

Paleomagnetists use the direction of the magnetization acquired in the Earth's ancient magnetic field to obtain estimates of the ancient latitude at which the rock formed. Calculation of a latitude relies on an assumption that the Earth's magnetic field is structured like a bar magnet when averaged over sufficiently long timescales, so that the magnetic field is vertical at the poles, and horizontal at the equator, also termed a Geocentric Axial Dipole (GAD). Estimates of the Earth's magnetic field direction, taken from different latitudes over the past 10 Myr conform relatively well to a GAD field, with a small hemispheric asymmetry (1). On the other hand, estimates of the Earth's magnetic field strength (the paleointensity) averaged over the last 5 Myr consistently show a behaviour incompatible with a strongly dipolar field. A seemingly persistent feature in paleointensity data is the presence of weak paleofields at high southern latitudes (2–4), which causes a hemispheric asymmetry in the paleointensity data. This is seen in paleointensities from the MagIC database over the last 5 Ma (plotted in Figure 1a) where the mean paleointensity at 80°S would be produced by a centered magnetic dipole with a moment of around 40 ZAm^2, whereas the mean paleointensity at 20°N would require a dipole moment with a magnitude closer to 80 ZAm^2. Attempts to fit Giant Gaussian Process (GGP) models to paleointensity data to determine the structure of the time-averaged field have found that the field consistently requires a strong quadrupole term 15-30% the strength of the dipole field (5, 6), producing this asymmetry. However, such a large quadrupole is completely incompatible with the directional data.

Three different hypotheses could explain the non-dipole like behaviour of global time-averaged paleointensity records: bias in paleointensity estimation, comparison of temporally distinct data in a time varying field, and genuine non-dipole field behavior. Regarding the issue of bias, paleointensity estimation involves normalizing the observed natural remanent magnetization (NRM) to a magnetization acquired in a known laboratory field. The accurate determination of a paleointensity therefore requires that the acquisition of a magnetization be reproducible. However, it has been shown (e.g., (7–10)) that some rocks have non reproducible magnetizations, which can lead to biased paleointensity estimates. Global paleointensity records may be confounded by these biased estimates, leading to an apparent non dipole signature. Alternatively, geomagnetic intensity variations through time

Significance Statement

Reconstructions of tectonic plates rely on the assumption that the time-averaged geomagnetic field behaves like a axial geocentric dipole. Global compilations of field directions are close to a GAD, but field strengths are not. Obtaining estimates of field strength is difficult because of high experimental failure rates and inconsistent analysis methods between studies. Here we present new data collected from igneous rocks in Hawai'i and use consistent analytical methods to compare them to published data from Antarctica and Israel. Our results indicate a persistent non-dipolar component in the Earth's magnetic field over the past 1.5 Ma, but more dipolar behavior prior to that. This is surprising, given our current understanding of the processes that give rise to the field.

Please provide details of author contributions here.

Please declare any competing interests here.

[2]To whom correspondence should be addressed. E-mail: bcychucsd.edu

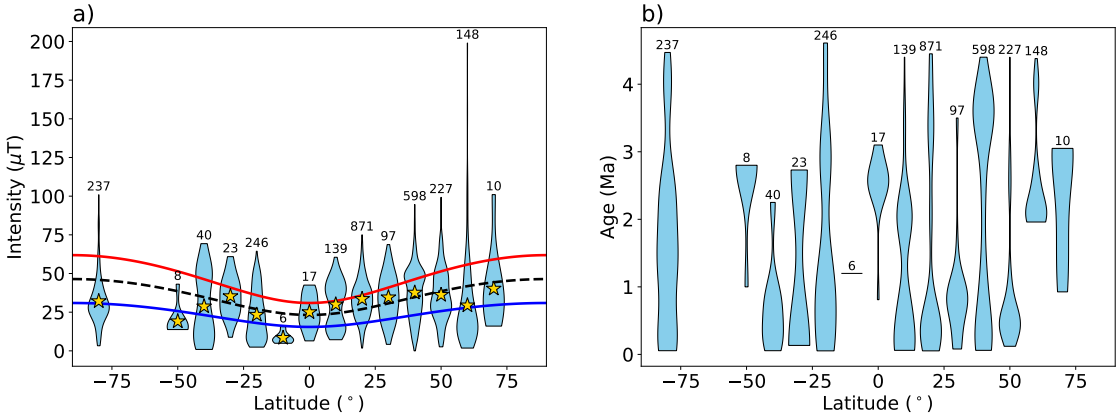

Fig. 1. Violin plots showing latitudinal binned distributions of a) paleointensity and b) age for reported paleointensity results from the MagIC database aged between 50 ka and 5 Ma. In a violin plot, the width of the violin represents the frequency of intensities in that latitude bin, with the widest point in the violin representing the modal value. The number of data points in each bin are noted above the violins. The yellow stars in a) are the mean paleointensity value at each latitude bin and the solid blue, dashed black and solid red lines represent the expected mean values for a dipole field with a strength of 40, 60 and 80 ZAm^2 respectively.

may not be well averaged. The majority of paleointensity determinations are made with volcanic rocks, which record an instantaneous snapshot of the magnetic field at the time they cool. Archeomagnetic data indicate that the Earth's magnetic field strength can vary strongly over decades to centuries (e.g., (11)), so numerous paleointensity estimates are necessary for a good average. If the field strength varies over long timescales (e.g. millions of years), then comparing the "average" of two studies may not be meaningful if the units sampled are of different ages. And finally, it is also possible that the geomagnetic field is not in fact GAD-like but has long-term non-axial dipole contributions (as suggested by (4, 12, 13)).

Paleomagnetists have identified behaviors in a paleointensity experiment that deviate from theoretical expectations and may lead to bias and recent studies have made a greater effort to eliminate such biased results. In most paleointensity studies, results from paleomagnetic specimens are excluded from the analysis if they fail a set of "selection criteria" which are phenomenological descriptions of these behaviors. Alternatively, the BiCEP method (14) attempts to find a relationship between the apparent paleointensity and one of these commonly used selection criteria (curvature (15)), and attempts to correct for the bias induced by the non-ideal behavior, obtaining accurate results without excluding data from the analysis based on arbitrary criteria. Recently, a study (4) which used the strict CCRIT criteria (16) and the BiCEP method on paleointensity studies from several latitudes found that there is still a discrepancy between these time-averaged paleointensities and those expected for a GAD field, making our first hypothesis (apparent non-dipole behavior is caused by bias in paleointensity estimation) unlikely to be the cause of inaccurate paleointensities.

Figure 1b shows the age distribution of latitudinally binned absolute paleointensity data in the MagIC database (without selection). It is apparent that different latitude bins have different age distributions. Because of this, the average paleointensity from each bin is representative of a different time period, and is not an average paleointensity for the whole of the last 5 Ma. High quality paleointensity data, analyzed in a consistent manner, are needed to determine whether temporal sampling is the cause of apparent non-dipolar behavior, or if the time-averaged field is truly non-dipolar, as outlined in our third hypothesis.

In this paper, we present paleointensity estimates from rapidly cooled volcanic material from lava flows, dikes and vent deposits (scoria and spatter cones) aged 0-4 Myr from the Hawai'ian islands. In Section 1, we describe how we collect samples in the field (1.A), how we conduct paleointensity experiments (1.B) on specimens therefrom, how we analyze our results using the BiCEP method which produces accurate estimates for specimens magnetized in known fields (1.C), and how we obtain ages for our samples using ^{40}Ar/^{39}Ar dating (1.D). In Section 2, we show the results of our paleointensity study in Hawai'i. Section 2.B discusses how our results suggest that scoria may be a useful lithology for obtaining high quality paleointensity estimates, and are in agreement with estimates from other lithologies. In Section 2.C we fit a model to our paleointensity data in an attempt to derive a time average that accounts for uneven temporal sampling. We then apply the same methodology to studies from Northern Israel and Antarctica. This allows us to test whether poor temporal sampling or non dipole behavior is responsible for the weaker paleointensity at high latitudes. Our results indicate that there is a persistent non-dipole component in the Earth's magnetic field over at least the past 1.5 Myr with older data being much more consistent with a GAD field.

1. Methods

A. Field Methods. Our results come from samples collected over three field seasons from outcrops on the Hawai'ian islands. Samples were collected from the islands of Hawai'i, Maui, Moloka'i, and O'ahu in an attempt to get a representative average paleointensity over the past 4 Myr. This study targeted predominantly glassy and fine grained igneous material from lava flow tops and bottoms, scoria cones and dike margins. Néel theory (18) predicts the physics of "uniaxial single domain" grains which should behave ideally in a paleointensity experiment. Only very small magnetic particle sizes exhibit single domain behavior, and so we sampled rapidly cooled materials most likely to contain these fine grains.

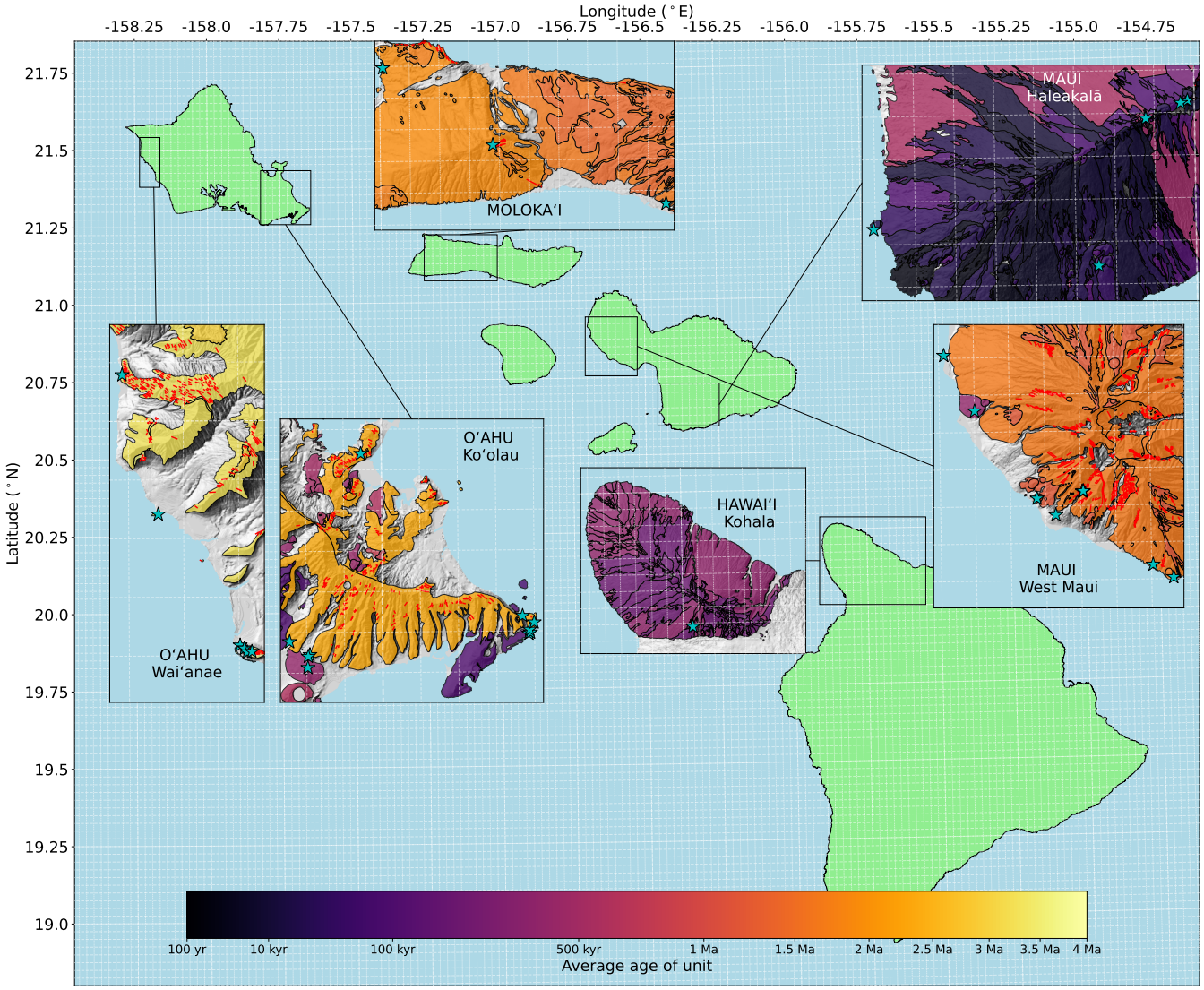

Fig. 2. Maps showing sampling localities for successful sites used in this study (blue stars). Insets are labeled with the name of each island in capital letters and the name of the volcano (if applicable) in lowercase. Each map shows samples from a different Volcano/Island. Colors represent ages of units (17), with darker colors indicating younger flows (see colorbar), and dike locations indicated by red lines. Topographic data: U.S. Geological Survey (USGS). 2015. USGS 10-m Digital Elevation Model (DEM): Hawai'i. Coastline data: Hawai'i Statewide GIS Program.

In the field, we collected small unoriented hand samples using a hammer and chisel; this allowed us to obtain smaller pieces of material and was less destructive than obtaining oriented specimens with a drill. Maps of our sampling localities are shown in Figure 2 and details regarding location, age and material are given in Table 1.

B. Laboratory Work. Each sample was crushed with a mortar and pestle to produce multiple paleomagnetic specimens with masses on the order of 0.1 g. Specimens were weighed and glued into 1 cm wide borosilicate glass tubes using a high temperature, low magnetic moment glue (KaSil). We subjected each specimen to the IZZI-Thellier method (21, 22). This is a step-wise double heating experiment in which the NRM is replaced by a Thermal Remanent Magnetization (TRM) acquired in a known lab field. Under the IZZI protocol, the order of the in-field and zero-field steps alternates at each temperature step. Under ideal conditions, the ratio of the magnetization lost in a zero-field step to the magnetization gained in an in-field step is the ratio of the ancient field (B_{anc}) to the laboratory field (B_{lab}). For this study, multiple lab fields were used for different specimens, as we observed that the choice of B_{lab} affected whether our specimens passed or failed some of our criteria (see Section 1.C).

C. Analysis of Data. To make sure that we have unbiased results, we used two different analysis methods on our data to obtain an estimate of the ancient field. Primarily, we used the BiCEP method (14) of estimating paleointensities, but we also looked at results using the CCRIT criteria of (16). BiCEP assumes that the magnetization records a single field, and thermochemical alteration of the specimen has not occurred. To make certain of this, we used the minimal selection criteria (see (23) for definitions and references), DANG<10, DRAT<10. In addition, we use a new parameter, MAD_{Coe}<5 which just uses the zero-field first steps. The set of temperature steps on the

Table 1. Ages and locations for sites from this study that passed CCRIT or BiCEP. Locations for all sites, including those that did not pass CCRIT or BiCEP are listed in the supporting information. Latitudes and Longitudes are referenced to the WGS84 standard.

Site	Island	Lithology	Lat. (°N)	Lon. (°E)	Age (Ma)	$\pm 2\sigma$
HW306	Hawai'i	Vent Deposit	20.04470	-155.73437	0.1900	0.0700
ML001	Moloka'i	Dike	21.13719	-157.15547	2.0700	0.0200
ML012	Moloka'i	Vent Deposit	21.08955	-157.01053	1.6100	0.0300
ML015	Moloka'i	Vent Deposit	21.19876	-157.24734	1.7700	0.0200
MU004	Maui	Vent Deposit	20.77605	-156.53433	1.4300	0.0200
MU009	Maui	Vent Deposit	20.81885	-156.61782	0.6100	0.0120
MU011	Maui	Vent Deposit	20.83016	-156.63110	1.2300	0.0690
MU012	Maui	Vent Deposit	20.88931	-156.67484	0.3000	0.0216
MU013	Maui	Vent Deposit	20.92685	-156.69633	0.5840	0.0100
MU023	Maui	Vent Deposit	20.61085	-156.31100	0.0765	0.0635
MU025	Maui	Vent Deposit	20.70692	-156.25424	0.0950	0.0450
MU027	Maui	Vent Deposit	20.70551	-156.25857	0.0950	0.0450
MU031	Maui	Vent Deposit	20.69669	-156.28040	0.0670	0.0404
MU036	Maui	Vent Deposit	20.63397	-156.45102	0.0106	0.0085
MU106	Maui	Dike	20.83446	-156.59879	1.4900	0.0500
MU109	Maui	Dike	20.83440	-156.59798	1.5500	0.0500
MU111	Maui	Dike	20.83471	-156.59808	1.4500	0.0600
MU113	Maui	Lava Flow	20.78467	-156.54893	1.1000	0.0600
OA003	O'ahu	Flow	21.29434	-157.81123	2.5500	0.0800
OA008	O'ahu	Flow	21.40440	-158.17461	3.7100	0.0600
OA014	O'ahu	Dike	21.51972	-158.22772	3.4900	0.1700
OA015	O'ahu	Flow	21.46033	-158.21154	3.1000	0.0300
OA019	O'ahu	Flow	21.30938	-157.65783	2.8400	0.0600
OA026	O'ahu	Flow	21.29836	-157.65380	2.7700	0.1300
OA028	O'ahu	Flow	21.29907	-157.65273	2.7200	0.0800
OA030	O'ahu	Vent Deposit	21.27831	-157.79929	0.3800	0.1100
OA100	O'ahu	Vent Deposit	21.28628	-157.79791	0.4800	0.0400
OA101	O'ahu	Vent Deposit	21.28521	-157.79900	0.4800	0.0400
OA104	O'ahu	Flow	21.30080	-157.65320	2.1800	0.3500
OA108	O'ahu	Dike	21.30527	-157.65027	2.2500	0.1700
OA114	O'ahu	Dike	21.41002	-157.76354	2.8700	0.0600
OA116	O'ahu	Dike	21.40308	-158.17264	3.7200	0.0500
OA117	O'ahu	Dike	21.40308	-158.17264	3.7200	0.0500
OA123	O'ahu	Sill Margin?	21.40149	-158.17141	2.5900	0.0900
OA124	O'ahu	Dike	21.40168	-158.16927	3.2500	0.0100

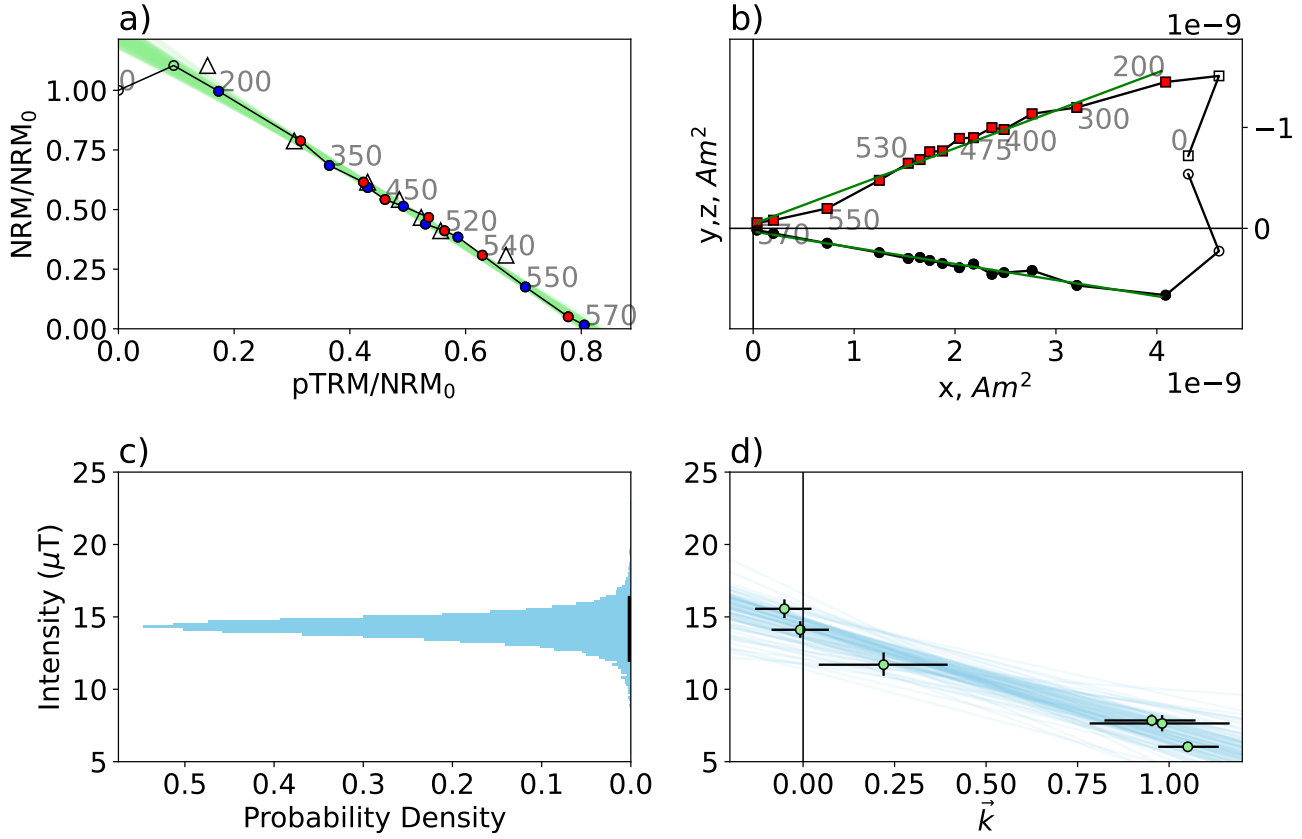

Fig. 3. Example of BiCEP being used to obtain a paleointensity for site MU111. a) Arai plot (19) for specimen MU111A05, red dots represent steps where the zero-field measurement was made first, and blue dots represent in-field first steps. Open circles represent temperature steps not used for this analysis. Triangles are pTRM checks and green curves are BiCEP's circular fits to the data. b) Zijderveld plot (20) showing magnetic direction data. Open symbols are steps where the temperature steps were not used. Green line is a principal component analysis fit to the directional data. c) Histogram of possible site mean intensities from BiCEP. d) BiCEP fit showing the predicted relationship (blue lines) between intensity (y axis) and the curvature criterion ($\vec{k}$, x axis).

Arai plot which maximize the FRAC criterion while passing the MAD$_{\mathrm{Coe}}$, DANG and DRAT criteria. The vast majority of our specimens pass these criteria with ease, and the ones that do not would unambiguously be rejected by almost any other set of criteria. Site results from BiCEP have a 95% credible interval which is equivalent to the full width of the 2σ interval from traditional selection criteria methods (e.g., CCRIT). We considered a site level result from BiCEP acceptable if it has a credible interval with a full width less than 40% of the median value, or 16 μT, whichever is greater (the original BiCEP A or B criteria of Cych et al. (2021) (14) only include the former criterion). This is equivalent to criteria of $\pm$10% or 4 μT used for the CCRIT at a site level. An example of BiCEP being used to estimate B_{anc} and its uncertainty for a site is shown in Fig. 3.

D. Age Constraints. We obtained a range of radiometric ages for our samples that span the past 4 Ma. Rocks from 23 of our successful sites were analyzed at the Argon Geochronology lab at Oregon State University (OSU) for age determination. 200-300 μm pieces from each sample were prepared by acid leaching in an ultrasonic bath according to the procedure of (24). This was followed by irradiation of the samples in the OSU TRIGA CLICIT nuclear reactor. Samples were then incrementally heated using a defocused CO_2 laser, and the isotopic composition of the released argon was measured using an ARGUS-VI multi-collector mass spectrometer. Seventeen of our ages were calculated using argon-argon (Ar-Ar) plateaus. Three ages from sites OA019, OA116 and OA124 were calculated using Mini-Plateau ages. Sites MU011 and MU036 were calculated using inverse isochron ages and site ML001 was calculated using a total fusion age. For sites OA030, OA100 and OA101, we used existing potassium-argon (K-Ar) ages, (25) and on West Maui, existing K-Ar ages (26) were similarly used for sites MU009 and MU013. Mapped scoria cones at sites MU023, MU025 and MU027 have good age constraints over the timescale we are interested in from K-Ar dating and stratigraphic relationships outlined in (27). Finally, site OA026 has its age constrained by stratigraphic relationship with our other Ar-Ar dated flows. A full table of ages is given in Table 1.

2. Results

Results are listed in Table 2. We obtain passing results from 35 sites (Table 2): 31 passed BiCEP and 21 passed CCRIT. Some of the results that pass CCRIT do not pass BiCEP, but those sites that pass both methods exhibit good agreement between one another. Because BiCEP gives a more objective analysis, and because we obtain more passing results with this

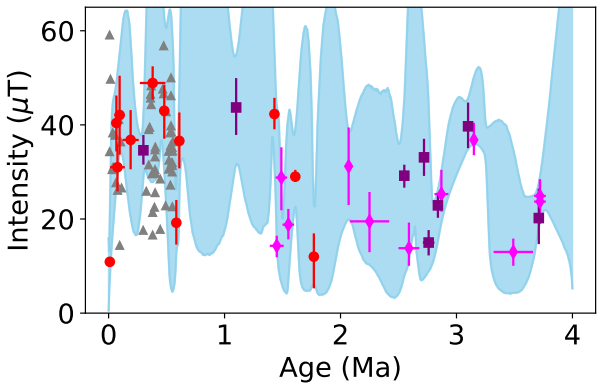

Fig. 4. Paleointensity and age estimates from this study using the BiCEP method from lava flows (purple squares), scoria cones (red circles) and dike margins (pink diamonds). Error bars represent the 95% credible interval for intensity estimates, and the 2σ interval for age estimates. Grey triangles are other Hawai'ian results from the HSDP2 core (28), which have a similar distribution over this time period to our results. Blue envelope represents the 95% credible interval for the AH-RJMCMC model (29) fit to the data (see section C).

method, we use only the results that pass BiCEP for the rest of our analyses.

We plot our results versus age in Fig. 4. It is apparent that our results support the hypothesis that the more recent field (over the past ∼1.5 Ma) is considerably higher than that from 1.5-4 Ma (e.g., (30)), supporting the hypothesis of a potential long period variation in the field strength (30–32). It is also worth noting that in Fig. 1, latitudes which have age distributions which skew towards ages older than 1 Ma (e.g. 80°S, 60°N, 0°) tend to have averages that agree with a ∼40 ZAm^2 dipole, whereas the majority of latitudes with mostly younger results tend to agree with a 60-70 ZAm^2 dipole moment, so qualitatively our hypothesis that the missing dipole may be caused by temporal sampling seems plausible. However, the data from Antarctica (3) span the entire last 4 Ma but also have an average field consistent with a 40 ZAm^2 axial dipole strength, so temporal sampling alone does not explain all of the deviation from a GAD field.

The high paleointensity results over the past 1.5 Ma come predominantly from vent deposits (scoria and spatter cones), whereas older results come predominantly from dikes and lava flows. The dikes and lava flows are associated with the early shield building stages of Hawai'ian volcanoes, whereas the vent deposits are predominantly from the later stages of volcanic construction. The difference in lithology being coupled with a difference in field strength may be concerning, however our young, high field strength results agree well with the average paleointensity from lava flows in the HSDP2 core ((28, 33), re-analyzed in (4)), shown as grey triangles in Figure 4, although the variance of the HSDP2 data is larger. Additionally, results from several scoria cones yielded much weaker fields, including for two cones on Moloka'i older than 1.5 Ma. This leads us to believe that our results from scoria are accurate.

3. Discussion

A. Pitfalls of selection criteria. We used the BiCEP method to obtain site level paleointensity estimates, and prefer this over the CCRIT method (and all other sets of selection criteria

Site	n_{pass}/n_{tot}	B_{min}	B_{anc}	B_{max}	Method
HW306	8/8	30.8	36.8	42.9	BiCEP
ML001	7/7	23.2	31.2	39.2	BiCEP
ML012	6/6	28.1	29.0	30.2	BiCEP
ML015	5/5	5.5	12.0	16.7	BiCEP
MU004	11/11	39.3	42.3	45.5	BiCEP
MU009	6/6	31.1	36.6	42.4	BiCEP
MU011	5/9	19.2	26.5	33.8	CCRIT
MU012	6/6	31.8	34.6	37.6	BiCEP
MU013	8/8	14.8	19.2	23.8	BiCEP
MU023	8/8	26.1	31.0	35.6	BiCEP
MU025	7/7	33.9	42.1	50.2	BiCEP
MU027	6/6	19.7	24.7	30.7	CCRIT
MU031	10/10	34.6	40.4	46.0	BiCEP
MU036	9/9	10.4	10.9	11.4	BiCEP
MU106	10/12	22.1	28.8	35.0	BiCEP
MU109	7/7	15.9	18.8	21.9	BiCEP
MU111	6/6	12.1	14.3	16.2	BiCEP
MU113	8/8	38.1	43.7	49.7	BiCEP
OA003	11/11	26.9	29.2	31.3	BiCEP
OA008	4/4	14.9	20.2	26.2	BiCEP
OA014	10/12	10.3	13.0	15.6	BiCEP
OA015	8/8	35.3	39.7	44.5	BiCEP
OA019	15/15	20.5	22.9	25.3	BiCEP
OA026	8/8	12.5	15.0	17.4	BiCEP
OA028	8/8	29.4	33.1	36.8	BiCEP
OA030	16/16	45.6	48.9	52.2	BiCEP
OA100	6/12	50.0	51.0	52.0	CCRIT
OA101	9/9	37.3	43.0	48.3	BiCEP
OA104	3/8	15.8	17.6	19.3	CCRIT
OA108	8/8	13.2	19.5	25.5	BiCEP
OA114	6/6	21.8	25.3	30.2	BiCEP
OA116	8/8	21.7	24.9	28.2	BiCEP
OA117	5/5	19.2	23.7	28.1	BiCEP
OA123	6/8	10.3	13.8	19.0	BiCEP
OA124	7/7	33.8	36.8	40.2	BiCEP

Table 2. Paleointensity results from specimens in this study which passed BiCEP and CCRIT. n_{pass}: Number of passing specimens. n_{tot}: Total number of specimens. For CCRIT results B_{min} and B_{max} represent the bounds of the 2σ interval, and so a full width of 40% or 16 μT is considered to have passed. The method column represents the preferred paleointensity result (BiCEP) when a site passed both BiCEP and CCRIT

in use by various authors) as BiCEP produces many more site level results than CCRIT. Often, BiCEP passed sites where specimens failed the FRAC criterion of CCRIT, which specifies that a large proportion of the total magnetization of the specimen is needed to make a paleointensity estimate. BiCEP accounts for the uncertainty in curvature (and therefore bias), introduced by using only part of a specimen's Arai plot for a paleointensity estimate. This can be seen in Fig. 3a, where specimen MU111A05 fails CCRIT due to low FRAC, but using a smaller part of the Arai plot translates to only a small increase in the uncertainty in curvature, shown by the green curves fit to the data.

In addition to the FRAC criterion in CCRIT, we identify cases in which criteria may reject a specimen if it has an ancient field much lower than the lab field. The MAD criterion may be exceeded if the laboratory magnetization acquired in an in-field step is not fully removed during a zero-field step, a consequence of a "high temperature pTRM tail" (34). This behavior is very noticeable in IZZI experiments (Fig. 5), as the in-field first steps are more strongly affected by this effect. This leads to a zig-zag appearance in the Zijderveld plot. The sizes of these tails are dependent on both the magnitude of the lab field, and the effect the tails have on MAD is dependent on the angle between lab and ancient field. If we call this angle θ, then the perpendicular part of the tails will be controlled by $B_{lab} \sin\theta$. If we assume no other sources of deflection to the MAD angle, the equation for the effect is:

$$\tan(\mathrm{MAD}) \propto \frac{B_{lab}}{B_{anc}} \sin\theta. \qquad [1]$$

This equation demonstrates that in the same lab field, sites with low ancient fields will be preferentially rejected with higher MAD, and sites with high ancient fields will be preferentially accepted.

To counteract the lab field-dependent effects, we used 10, 30 and 70 μT fields in our studies, which captures the range of the ancient field. At some sites with low estimated B_{anc}, there was an observably higher pass rate in lower fields. An example of this for site OA014 is illustrated in Fig. 5. To treat specimens magnetized in different fields fairly, it is tempting to come up with a criterion for MAD which is dependent on Equation 1. However, effects that we may be using MAD to look for (e.g. two component magnetizations) will not be dependent on the lab field, and so we suggest calculating MAD for exclusively the zero-field first or "Coe" type steps (35). Although pTRM tails may still be present in these steps, they will be significantly reduced in in-field first steps. We call a MAD calculated using these steps $\mathrm{MAD_{Coe}}$ and how it compares to MAD for site OA014 is shown in Fig. 5d. This significantly reduces the lab field-dependent effects, but does not eliminate them entirely. Because pTRMs scale with the lab field used, there may be other unrecognized pTRM dependent effects. We recommend using a range of lab fields in paleointensity studies as the most robust way of compensating for these effects.

B. Sample Characterization. We have demonstrated our ability to obtain high quality paleointensity results from our samples using the BiCEP method. However, it is not clear what the primary carriers of the magnetization are for these samples, particularly for samples from vent deposits, which are relatively unstudied in the paleointensity literature. To attempt

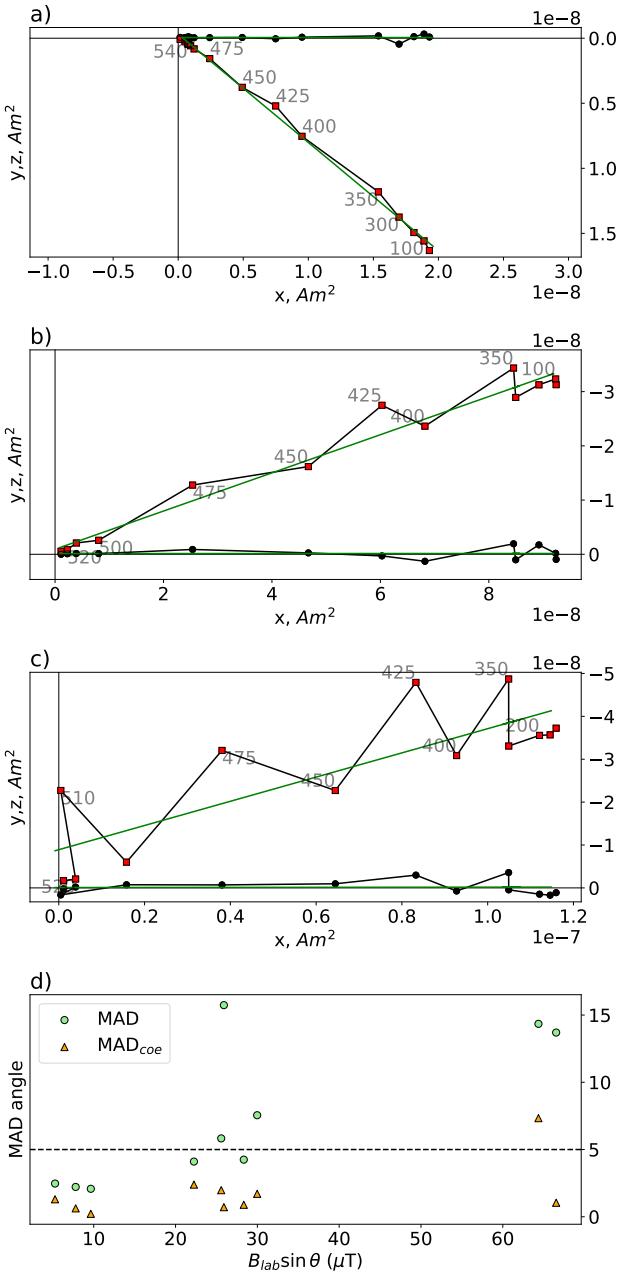

Fig. 5. a)-c) Zijderveld plots of specimens from site OA014, showing zig-zagging behavior that progressively increases with lab field and d) Scatter plot showing the relationship between the MAD criterion, and the magnitude and angle of the lab field for all ten fully demagnetized specimens from this site. Paleointensity experiments were performed laboratory fields of a) a 10 μT, b) 30 μT and c) 70 μT. d) MAD (green circles) angle against the strength of the component of the lab field perpendicular to the ancient field direction (calculated by the PCA of the zero-field first steps). Orange triangles are the MAD of the zero-field first steps only ($\mathrm{MAD_{Coe}}$). Horizontal dashed line represents the selection criterion (5) used in this study. Using $\mathrm{MAD_{Coe}}$ improves, though does not completely eliminate, the lab-field dependence of MAD. All MADs were calculated using temperature steps above 400-600°C to avoid any potential viscous remanent magnetization (VRM).

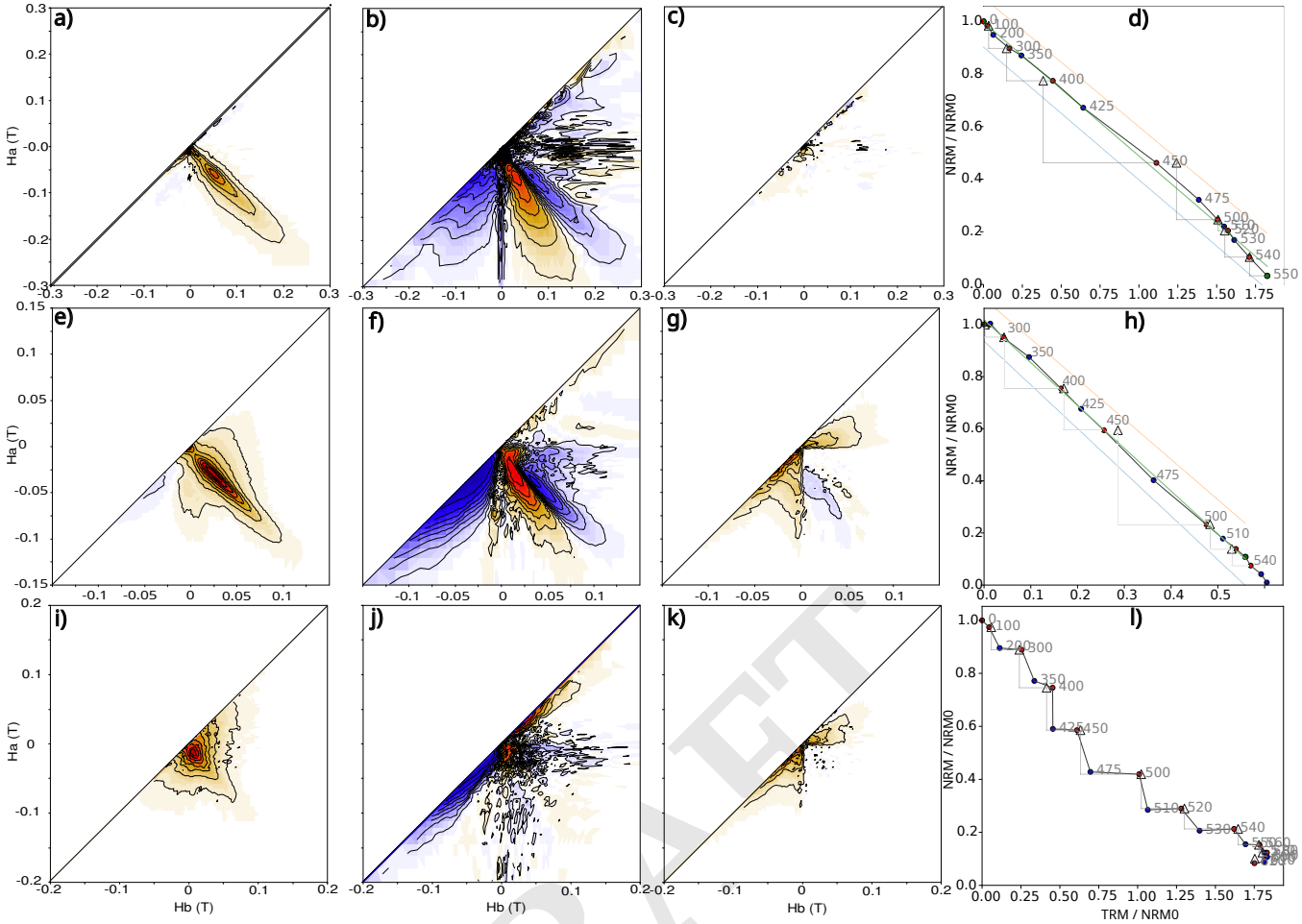

Fig. 6. First Order Reversal Curves (FORCs) a),e),i), iFORCs b),f),j), and tForcs c),g),j) calculated using the xFORC protocol (36). All FORCs calculated using a smoothing factor of 2 and a non-linear color scale of 1, except for iFORCs which were calculated using a smoothing factor of 3 and a non-linear color scale of 10. Arai plots are plotted in d),h),k). FORCs use sister specimens from two sites that yielded passing results: OA030 (top row), OA014 (center row) and a site which did not pass CCRIT or BiCEP, HW305 (bottom row). Sites which yielded specimens with linear Arai plots tend to have an elongated central ridge and have 3 lobes in the iFORC (top and center rows), whereas sites with curved Arai plots tend to have more spread along the $H_a = H_b$ direction and have extremely noisy iFORCs with little information.

to characterize the domain state of our samples, we obtained First Order Reversal Curves (FORCs, (37)) using the xFORC protocol of (36) on selected material from sites which passed BiCEP (and from some which failed). For this analysis we used sister specimens from the same samples for which the paleointensity results were acquired. FORCs are a qualitative way of assessing the domain state of a specimen using its hysteresis properties. Specimens which contain "Single-Domain" (SD) grains which are ideal for the paleointensity experiment will have FORCs with a central ridge of positive values along the H_a=-H_b axis (see e.g. Fig. 6a). Specimens with higher numbers of non SD grains will have FORCs which have a spread along the H_a=H_b axis. The iFORC which represents the induced part of the magnetization displays a pattern of three distinct "lobes" (e.g. Fig 6b,e) for a sample containing SD grains, whereas it may display four "lobes" or be extremely noisy for samples containing non-SD grains. The tFORC represents "transient hysteresis" which occurs in non-SD grains; specimens with just noise on the tFORC (e.g. Fig. 6c) are most likely to be single domain.

Examples of FORCs and Arai plots for different samples are displayed in Fig. 6. The FORC interpretations generally agree with the paleointensity experimental results. FORCs obtained from dike samples have pronounced central ridges and three lobes in the iFORC if visible, and effectively no tFORC (Fig. 6a-d). These samples generally had Arai plots which were straight lines, but sometimes underwent thermochemical alteration at high temperatures. Samples from lava flows and vent deposits had central ridges, with small amounts of transient hysteresis and spreading along the $H_a = H_b$ axis. These samples still have linear Arai plots, and often have three lobes present in the iFORC, which suggests that the majority of carriers in these specimens are single domain (see Fig. 6e-h). An example from a relatively coarse grained lava flow is given in Fig. 6i-l. Samples like these had highly curved or zig-zagging Arai plots (Fig. 6l) generally had no central ridge and lots of spreading along the $H_a = H_b$ axis (Fig. 6i). These samples had pronounced tFORCs(Fig. 6k) , and only noise in the iFORCs away from the H_a axis (Fig. 6j), observations which are consistent with the curved and zig-zagging Arai plots.

We also obtained Back Scattered Electron (BSE) images using an Scanning Electron Microscope (SEM), and Electron Dispersive X-Ray Spectroscopy (EDS) element maps to iden-

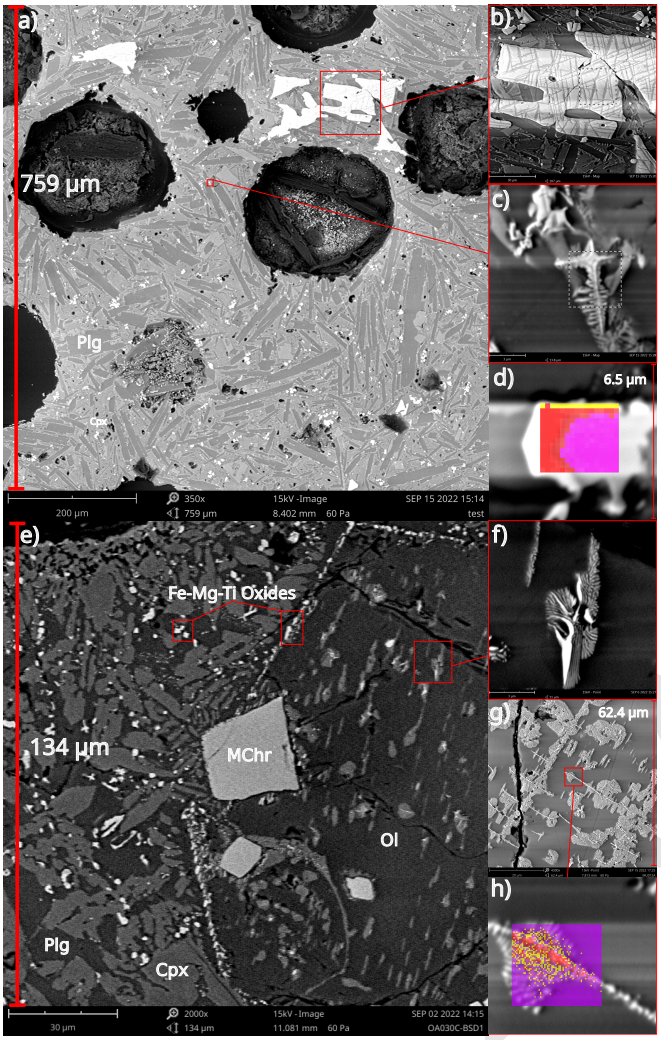

Fig. 7. Back Scattered Electron (BSE) images and Electron Dispersive X-Ray Spectroscopy (EDS) maps of sister specimens from selected samples used in this study. Red text gives vertical field of view (FOV) for each image. a) BSE image of sample ML015A, a scoria vent deposit. b) Zoomed in image of large oxide in a), showing Fe-Ti exsolution textures. c) Zoomed in image of small oxide in a), showing elongate skeletal/cruciform structure. d) EDS element map of a typical oxide from another scoria vent deposit, ML012A, showing heterogeneous composition in the Iron-Titanium oxides. The atomic content of Si is shown in yellow, Fe in red, and Ti in pink. e) BSE image of sample OA030A, an agglutinated basanite vent deposit. f) Close up of high temperature alteration texture in olivine phenocryst. g) The same texture present in sample MU012A, a breccia from the bottom of a basanite lava flow. h) Close up of this texture with EDS element map. Colors are the same as d), with purple representing Mg. Note that the light colors in the BSE image represent an iron rich phase (interpreted as magnetite), which is surrounded by a phase richer in silicon than the surrounding olivine, interpreted as enstatite. Dominant mineral phases written on a) and e): Plg: plagioclase feldspar, Cpx: clinopyroxene, Ol: olivine, MChr: chrome spinel. Horizontal banding present in b),c),d),f),h) is an artifact of charging the sample that occurs in the SEM's EDS element mapping mode.

tify iron oxides in several thin sections taken from our samples. Several pictures from these analyses are displayed Fig. 7. Dike samples we analyzed contained no visible iron oxides in the glass, and almost no iron oxides in the groundmass. This is consistent with our FORCs and Arai plots (Fig. 6a-d), which are indicative of this specimen containing a predominance of single domain grains, which are 10s of nm in scale and not resolvable by the SEM used in this analysis. By contrast, samples from vent deposits contained numerous micron-scale iron bearing oxides in the groundmass, and in some cases, larger iron oxides on the scales of 100s of microns (Fig. 7a-d), size ranges where we would expect the grains to yield curved Arai plots. Many of these grains have elongated "cruciform" textures (Fig. 7c) or have heterogeneous compositions (Fig. 7a,d). One possibility is that these textures may persist to smaller scales, causing the larger grains to behave like assemblages of smaller, single domain, grains, due to their elongation or having smaller magnetic subregions separated by nonmagnetic lamellae. Another possibility is that these large grains do not contribute to the remanence. However, the lava flows and vent deposits have much higher NRM moments than the dikes, with mass normalized NRMs on the order of 10^{-2} to 10^{-3} Am^2/kg, as opposed to the dikes which have moments on the order of 10^{-4} to 10^{-5} Am^2/kg.

Two thin sections from sites MU012 and OA030 have numerous olivine grains which exhibit an unusual texture, as displayed in Fig. 7e-h. This texture has been observed previously (38, 39) and is interpreted as being caused by oxidation of olivine at temperatures above 800°C, which causes breakdown into an iron oxide (magnetite or hematite depending on formation conditions) and enstatite (see Fig. 7h and figure caption). The temperature of the oxidation means that the samples were oxidized prior to gaining a magnetization, which means the NRM is a primary TRM acquired during cooling. Oxidation of this kind seems to typically occur in fire fountaining strombolian type eruptions e.g. (40) where the lavas remain at high temperatures in an oxidizing environment for a while (e.g. 950 °C for 24-48 hours as per (41)). OA030 is an agglutinated basanitic vent deposit, agreeing with this oxidative environment, whereas the MU012 sample was taken from breccia/clinkers in an a'ā lava flow, which may also undergo high temperature oxidation although the source is less clear.

Both sites with evidence for high temperature oxidation of olivines had highly linear Arai plots (see Figure 6h), with 16/16 specimens passing the strict CCRIT criteria for OA030, and 6/6 passing for MU012. Additionally a sample from OA030 has a FORC indicative of single-domain to single-vortex domain state, with a central ridge and three lobes in the iFORC (see Fig. 6, middle row). This indicates that the oxides formed by this breakdown may have extremely desirable properties for paleointensity experiments. Similar to the smaller oxides found in our other vent deposits (Fig. 7c), the elongation and finger-like structures present in these oxides could also explain their ideal behavior in the paleointensity experiment. These thin sections also contained numerous micron scale iron-titanium-magnesium oxides (interpreted as magnesioferrite) in the groundmass and around the outside of the olivine grains (Fig. 7e), but because the majority of the remanence unblocks between 400 and 600°C (see Fig. 6d), we believe that magnetite is the dominant remanence carrier in these specimens.

Despite the large iron oxides observed in vent deposits and

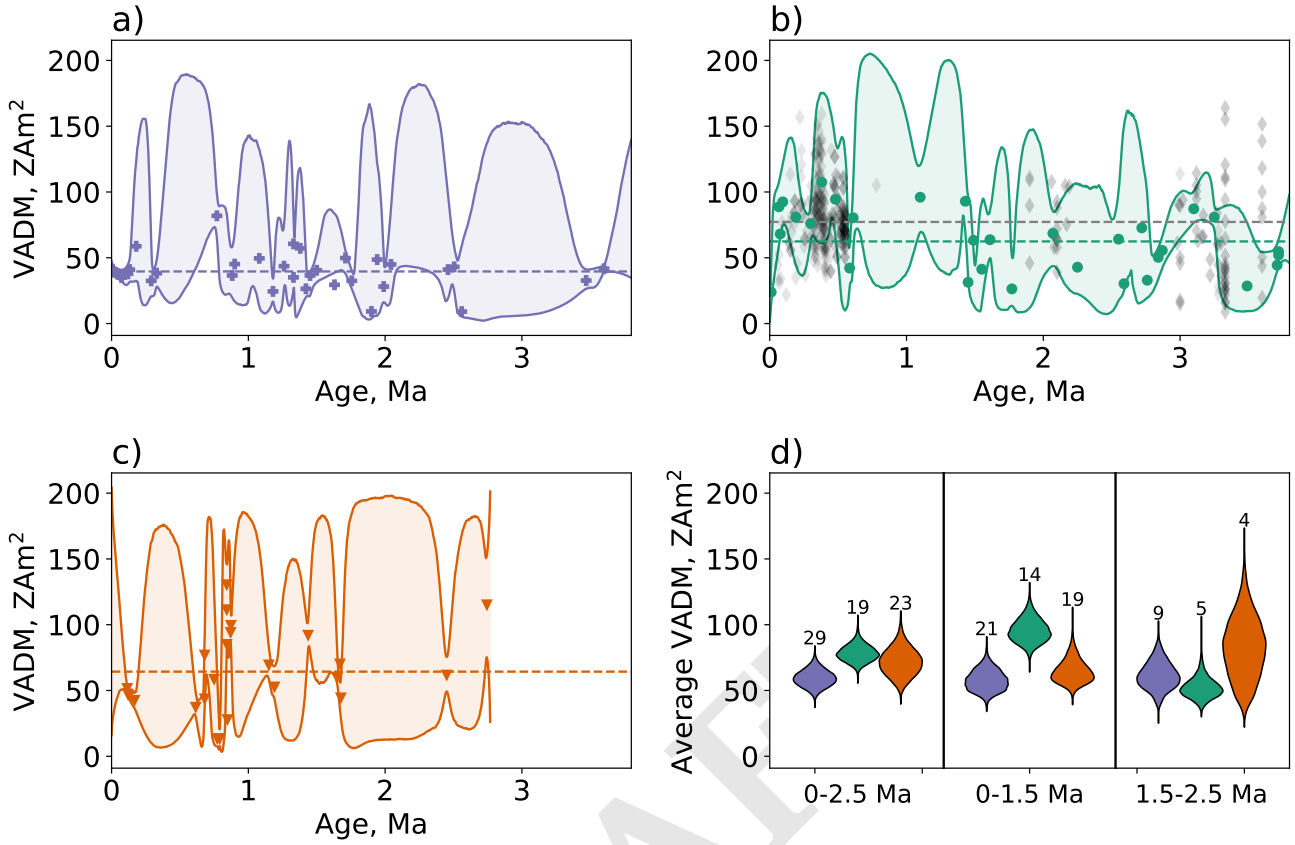

Fig. 8. a) - c) Plots of VADM against age (symbols), and 95% credible envelopes for AH-RJMCMC models (29) (shaded areas) for studies from a) Antarctica (purple plus symbols), b) Hawai'i (green dots), and c) Israel (orange triangles). Horizontal dashed lines are the average VADM of all paleointensity estimates (symbols) for each plot. In b), all unfiltered data in the MagIC database from Hawai'i aged between 50 ka and 3.8 Ma are plotted as grey diamonds, and the average VADM from these data are plotted as a grey horizontal line. d) Violin plots showing the distribution of averaged VADMs over different time periods, numbers refer to the number of paleointensity within these temporal ranges, although data outside these ranges may also contribute to these averages. Data from Hawai'i have a significantly higher average VADM than in Israel and Antarctica over the past 1.5 Ma, which is reflected in the averages from 0-2.5 Ma. Average VADMs for data older than 1.5 Ma appears to agree for all three locations.

lava flows from this study, we conclude that these lithologies provide a good source for paleointensity estimates, as they have a high success rate relative to our other lithologies owing to their strikingly linear Arai plots (see Fig. 6, top row). Site MU113 provides further evidence for this, as material sampled from the inside of a lava tube gave an identical result to material sampled from a scoriaceous bomb entrained in the same flow. There are other reasons to favour these types of lithologies: The formation of these samples in an oxic environment at high temperature may help prevent thermochemical alteration during the paleointensity experiment, and fresh scoria is also easy to come by in Hawai'i, as many scoria cones are quarried. However, most preserved vent deposits are typically formed during the later stages of Hawai'ian volcanism, and consequently we have no results from scoria older than 2 Ma.

C. Temporal Distributions of Intensity. Mismatch between the observed distribution of paleointensities with latitude and the expected distribution for a GAD field Fig 1a) could potentially be caused by inconsistencies in treatment of data among different paleointensity studies. To compare the time-averaged field from our model to data from different latitudes, we reanalyzed results from recent paleomagnetic studies in Northern Israel (4) and Antarctica (3) using the BiCEP method and the same criteria used for the Hawai'i samples. Tables of results from these re-analyses can be found in the Supporting Information. Each of these studies yielded passing sites with results spanning the past 2.5 Myr. For direct comparisons between locations, we convert each paleointensity result to a Virtual Axial Dipole Moment (VADM) which is the moment of the geocentric dipole (measured in ZAm^2) that would yield the observed paleointensity at a given latitude. Our average VADM for Hawai'i is 62.4 ZAm^2, which is similar to the 64.2 ZAm^2 value from Israel, but is significantly higher than the average in Antarctica (39.6 ZAm^2). Plots of VADMs with age for each location are shown in Figures 8a)-c), with average VADMs plotted as horizontal dashed lines. In Figure 8b we also plot all the data from Hawai'i in the MagIC database from this time interval in grey. The unfiltered data have a significantly higher variance than our data, and the weaker field seen prior to 1.5 Ma in our data is not apparent in the unfiltered Hawai'ian data, which have an average VADM of 77.2 ZAm^2. These differences could occur because more field variation is being captured by the larger dataset, or because the unfiltered data have more variance due to inconsistency in their analysis (for example, preferentially taking the low

temperature steps in a potentially sagging Arai plot). Despite the consistency in analysis of our data, the average VADM in Hawai'i and Israel is still very different to that found in Antarctica, indicating that inconsistency in analyses and biased paleointensities caused by Arai plot curvature are not the source of this mismatch.

Taking an average VADM of the entire age range of our data may not be representative of the time-averaged field, because our data have different temporal distributions, with no data in Israel older than 2.75 Ma. In Hawai'i, this average does not capture the change in average field strength seen at 1.5 Ma, and in Israel, we have many paleointensity data which record a strong field and come from a small range of time around 850 ka B.P. Because this time interval is oversampled, it will bias our average VADM towards these higher values. To account for these problems, it would make sense to fit a curve to our VADMs and take an average of the curve over an interval of interest. We do this using the "Age Hyperparameter Reversible Jump Markov Chain Monte Carlo" (AH-RJMCMC) method (29). This model fits piecewise linear curves to paleointensity data in a probabilistic fashion, with curves with less linear pieces being preferable for the model. At times when there are few data, the model uncertainties become very large and revert to a uniform prior distribution, which we set as 0-220 ZAm^2. At times where we have no data, the uncertainty in the average VADM will increase, and so any differences in the average VADM using this method are driven by the data.

We computed the AH-RJMCMC models, which output a series of possible piecewise linear curves at each locality. We took the average value of each curve over the past 2.5 Ma, and converted these averages to VADMs. The models produced by this analysis are shown in Fig. 8a-c, and the distributions of the time-averaged VADMs for each locality are plotted on the violin plots in Figure 8d. Using this methodology, it is apparent that the time-averaged VADMs over the last 1.5 Ma from Hawai'i and Antarctica are indeed not consistent with each other, but the time-averaged VADM in Israel could be compatible with either of the other latitudes. However, there is not enough evidence to confirm a difference in the temporal average between Hawai'i and Antarctica from 1.5-2.5 Ma, with the average VADMs appearing consistent. This implies that poor temporal sampling is not the reason for inconsistent paleointensities at different latitudes, but that some form of genuine non-dipolar field behavior that causes higher fields in Hawai'i than Antarctica at least since 1.5 Ma. More paleointensity studies with high quality paleointensity data at different latitudes (especially from the southern hemisphere) are needed to better understand the sources of this non-dipolar behavior.

Conclusions

In this paper, we obtained 31 high quality paleointensity results from dikes, lava flow tops and vent deposits collected in the Hawai'ian islands, with ages ranging from 0-4 Ma. We demonstrate a methodology for obtaining accurate time-averaged paleointensities, with uncertainties which allow direct comparison between paleointensity studies at different latitudes. The use of BiCEP allows for consistent comparison of results between different studies, and using the methodology of Livermore et al. (2018) (29) allows us to obtain a time-averaged intensity, with uncertainty, which accounts for the temporal distribution of our paleointensity. Because these robust statistical approaches are used for calculating time-averaged paleointensities, we are able to exclude the hypotheses that inconsistency of our time-averaged VADMs is due to either biased paleointensity data, or inconsistent temporal sampling of paleointensities.

Applying the new methodology to data from the Hawai'ian islands, we find that the time-averaged paleointensity in Hawai'i over the past 1.5 Ma was higher than during the period from 1.5-4 Ma. Comparing results from paleointensity studies at three latitudes, we find that this period of high paleointensity is not recorded in rocks from Antarctica or Israel. We reiterate the conclusion of other recent papers (e.g. (4)) that the Earth's magnetic field averaged over the past 1.5 Ma does not conform to a Geocentric Axial Dipole. Further time averages at a greater range of latitudes and times will be needed to obtain better estimates of the structure of this time-averaged field.

Our results also indicate that vent deposits containing scoria and olivine bearing rocks which are oxidized at high temperatures are potentially good lithologies for obtaining high quality paleointensity estimates, with higher success rates in the paleointensity experiment. Specimens from these lithologies have strong magnetizations and tend to alter less in paleointensity experiments. Additionally, these deposits are frequently quarried, allowing for easy access to fresh material in the field. Despite their useful properties in paleointensity experiments, and their single-domain like FORCs, the size of iron oxides in these samples when viewed under a microscope is orders of magnitude larger than would be expected for single domain grains. Further study of the magnetic carriers in these samples should be undertaken to understand why they have such ideal rock magnetic properties.

References.

1. G Cromwell, CL Johnson, L Tauxe, CG Constable, NA Jarboe, PSV10: A Global Data Set for 0–10 Ma Time-Averaged Field and Paleosecular Variation Studies. *Geochem. Geophys. Geosyst.* **19**, 1533–1558 (2018).
2. KP Lawrence, et al., Paleomagnetic field properties near the southern hemisphere tangent cylinder. *Geochem. Geophys. Geosyst.* **10**, Q01005 (2009).
3. H Asefaw, L Tauxe, AAP Koppers, H Staudigel, Four-Dimensional Paleomagnetic Dataset: Plio-Pleistocene Paleodirection and Paleointensity Results From the Erebus Volcanic Province, Antarctica. *J. Geophys. Res. Solid Earth* **126**, e2020JB020834 (2021).
4. L Tauxe, H Asefaw, N Behar, AAP Koppers, R Shaar, Paleointensity Estimates from the Pleistocene of Northern Israel: Implications for hemispheric asymmetry in the time-averaged field. *Geochem. Geophys. Geosyst.* **n/a**, e2022GC010473 (2022).
5. AR Muxworthy, Considerations for Latitudinal Time-Averaged-Field Palaeointensity Analysis of the Last Five Million Years. *Front. Earth Sci.* **0** (2017).
6. VP Shcherbakov, AV Khokhlov, NK Sycheva, Analysis of the Hypothesis of a Giant Gaussian Process as a Means for Describing Secular Variations of the Geomagnetic Field Vector. *Izv. Phys. Solid Earth* **55**, 182–194 (2019).
7. S Levi, The effect of magnetite particle size on paleointensity determinations of the geomagnetic field. *Phys. Earth Planet. Inter.* **13**, 245–259 (1977).
8. D Dunlop, O Özdemir, Beyond Néel's theories: thermal demagnetization of narrow-band partial thermoremanent magnetization. *Phys. Earth Planet. Int.* **126**, 43–57 (2001).
9. D Krása, C Heunemann, R Leonhardt, N Petersen, Experimental procedure to detect multidomain remanence during thellier–thellier experiments. *Phys. Chem Earth (A/B/C)* **28**, 681 – 687 (2003) Paleo, Rock and Environmental Magnetism 2002.
10. L Tauxe, et al., Understanding Nonideal Paleointensity Recording in Igneous Rocks: Insights From Aging Experiments on Lava Samples and the Causes and Consequences of "Fragile" Curvature in Arai Plots. *Geochem. Geophys. Geosyst.* **22**, e2020GC009423 (2021).
11. R Shaar, et al., Synchronizing archaeomagnetic field intensity records in the levant between the 23^{rd} and 15^{th} cennturies bce: chronological and methodological implications. *Geochem. Geophys. Geosystems* **21**, e2020GC009251 (2020).
12. RL Wilson, Permanent Aspects of the Earth's Non-dipole Magnetic Field over Upper Tertiary Times. *Geophys. J. Int.* **19**, 417–437 (1970).
13. G Cromwell, et al., In search of long-term hemispheric asymmetry in the geomagnetic field: Results from high northern latitudes. *Geochem. Geophys. Geosyst.* **14**, 3234–3249 (2013).
14. B Cych, M Morzfeld, L Tauxe, Bias Corrected Estimation of Paleointensity (BiCEP): An Improved Methodology for Obtaining Paleointensity Estimates. *Geochem. Geophys. Geosyst.* **22**, e2021GC009755 (2021).

15. GA Paterson, A simple test for the presence of multidomain behavior during paleointensity experiments. *J. Geophys. Res. Solid Earth* **116** (2011).
16. G Cromwell, L Tauxe, H Staudigel, H Ron, Paleointensity estimates from historic and modern Hawaiian lava flows using glassy basalt as a primary source material. *Phys. Earth Planet. Inter.* **241**, 44–56 (2015).
17. DR Sherrod, JM Sinton, SE Watkins, KM Brunt, Geologic map of the state of hawaii. *US geological survey open-file report* **1089**, 83 (2007).
18. L Néel, Théorie du traînage magnétique des ferromagnétiques en grains fins avec applications aux terres cuites. *Ann. géophys.* **5**, 99–136 (1949).
19. T Nagata, Y Arai, K Momose, Secular variation of the geomagnetic total force during the last 5000 years. *J. Geophys. Res.* **68**, 5277–5282 (1963).
20. JDA Zijderveld, *A.C. demagnetization of rocks: Analysis of results*, Methods in Paleomagnetism. (Chapman and Hall), (1967).
21. L Tauxe, H Staudigel, Strength of the geomagnetic field in the Cretaceous Normal Superchron: New data from submarine basaltic glass of the Troodos Ophiolite. *Geochem. Geophys. Geosyst.* **5** (2004).
22. Y Yu, L Tauxe, A Genevey, Toward an optimal geomagnetic field intensity determination technique. *Geochem. Geophys. Geosyst.* **5** (2004).
23. G Paterson, L Tauxe, A Biggin, R Shaar, L Jonestrask, On improving the selection of thellier-type paleointensity data. *Geochem. Geophys. Geosystems* **15** (2014).
24. AAP Koppers, H Staudigel, JR Wijbrans, Dating crystalline groundmass separates of altered Cretaceous seamount basalts by the 40Ar/39Ar incremental heating technique. *Chem. Geol.* **166**, 139–158 (2000).
25. A Ozawa, T Tagami, MO Garcia, Unspiked K–Ar dating of the Honolulu rejuvenated and Ko'olau shield volcanism on O'ahu, Hawai'i. *Earth Planet. Sci. Lett.* **232**, 1–11 (2005).
26. T Tagami, Y Nishimitsu, DR Sherrod, Rejuvenated-stage volcanism after 0.6-m.y. quiescence at West Maui volcano, Hawaii: new evidence from K–Ar ages and chemistry of Lahaina Volcanics. *J. Volcanol. Geotherm. Res.* **120**, 207–214 (2003).
27. DR Sherrod, Y Nishimitsu, T Tagami, New K-Ar ages and the geologic evidence against rejuvenated-stage volcanism at Haleakala, East Maui, a postshield-stage volcano of the Hawaiian island chain. *GSA Bull.* **115**, 683–694 (2003).
28. S Cai, L Tauxe, G Cromwell, Paleointensity From Subaerial Basaltic Glasses From the Second Hawaii Scientific Drilling Project (HSDP2) Core and Implications for Possible Bias in Data From Lava Flow Interiors. *J. Geophys. Res. Solid Earth* **122**, 8664–8674 (2017).
29. PW Livermore, A Fournier, Y Gallet, T Bodin, Transdimensional inference of archeomagnetic intensity change. *Geophys. J. Int.* **215**, 2008–2034 (2018).
30. L Tauxe, Long-term trends in paleointensity: The contribution of dsdp/odp submarine basaltic glass collections. *Phys. Earth Planet. Interiors* **156**, 223–241 (2006).
31. P Selkin, L Tauxe, Long-term variations in paleointensity. *Phil. Trans. Roy. Soc. Lond.* **358**, 1065–1088 (2000).
32. L Ziegler, C Constable, CL Johnson, L Tauxe, Padm2m: a penalized maximum likelihood model of the 0-2 ma paeomagneitc axial dipole moment. *Geophys. J. Int.* **184**, 1069–1089 (2011).
33. L Tauxe, JJ Love, Paleointensity in Hawaiian Scientific Drilling Project Hole (HSDP2): Results from submarine basaltic glass. *Geochem. Geophys. Geosyst.* **4** (2003).
34. D Dunlop, O Özdemir, Effect of grain size and domain state on thermal demagnetization tails. *Geophys. Res. Lett.* **27**, 1311–1314 (2000).
35. RS Coe, The determination of paleo-intensities of the earth's magnetic field with emphasis on mechanisms which could cause non-ideal behavior in thellier's method. *J. Geomag. Geoelectr.* **19**, 157–178 (1967).
36. X Zhao, et al., Magnetic domain state diagnosis using hysteresis reversal curves. *J. Geophys. Res. Solid Earth* **122**, 4767–4789 (2017).
37. C Pike, A Roberts, K Verosub, Characterizing interactions in fine magnetic particle systems using first order reversal curves. *J. Appl. Phys.* **85**, 6660–6667 (1999).
38. T Ejima, et al., Precipitates within olivine phenocrysts in oxidized andesitic scoria from Kasayama volcano, Hagi, Japan. *J. Miner. Petrol. Sci.* **112**, 116–126 (2017).
39. MS Blondes, MT Brandon, PW Reiners, FZ Page, NT Kita, Generation of Forsteritic Olivine (Fo99·8) by Subsolidus Oxidation in Basaltic Flows. *J. Petrol.* **53**, 971–984 (2012).
40. S Del Moro, A Renzulli, P Landi, S La Felice, M Rosi, Unusual lapilli tuff ejecta erupted at Stromboli during the 15 March 2007 explosion shed light on the nature and thermal state of rocks forming the crater system of the volcano. *J. Volcanol. Geotherm. Res.* **254**, 37–52 (2013).
41. SE Haggerty, I Baker, The alteration of olivine in basaltic and associated lavas. *Contrib. Miner. Petrol.* **16**, 233–257 (1967).

Data Archival. All data and interpretations are available at https://earthref.org/MagIC/19614/9208acad-0f62-4d9e-b265-4c8907d40eb7 and will be made available in the MagIC database at earthref.org/MagIC/19614 on acceptance of this paper. Python notebooks for producing figures can be found at https://github.com/bcych/hawaiian_paleointensity .

ACKNOWLEDGMENTS. This work was partially supported by EAR1827263 to LT and EAR1520788 to GC. We would like to thank the Hawai'i Department of Land and Natural Resources' Forestry and Wildlife Program for issuing sampling permits in West Maui, and Moloka'i Ranch Ltd. and Moloka'i Land Trust for allowing us to sample on their land. We are grateful for comments from Cathy Constable and Jeffery Gee which improved the manuscript. Finally we would like to thank the late Jasper Konter for his help in the field and hospitality during our field work on Oahu. He will be missed.

Supporting Information for

Changes in non-dipolar field structure over the Plio-Pleistocene: New paleointensity results from Hawai‘i compared to global datasets

Brendan Cych[a], Lisa Tauxe[a], Geoff Cromwell[b], John Sinton[c], and Anthony A.P. Koppers[d] 1

[a]University of California, San Diego; [b]Occidental College; [c]University of Hawai'i at Manōa; [d]Oregon State University

Brendan Cych. E-mail: bcych@ucsd.edu

This PDF file includes:

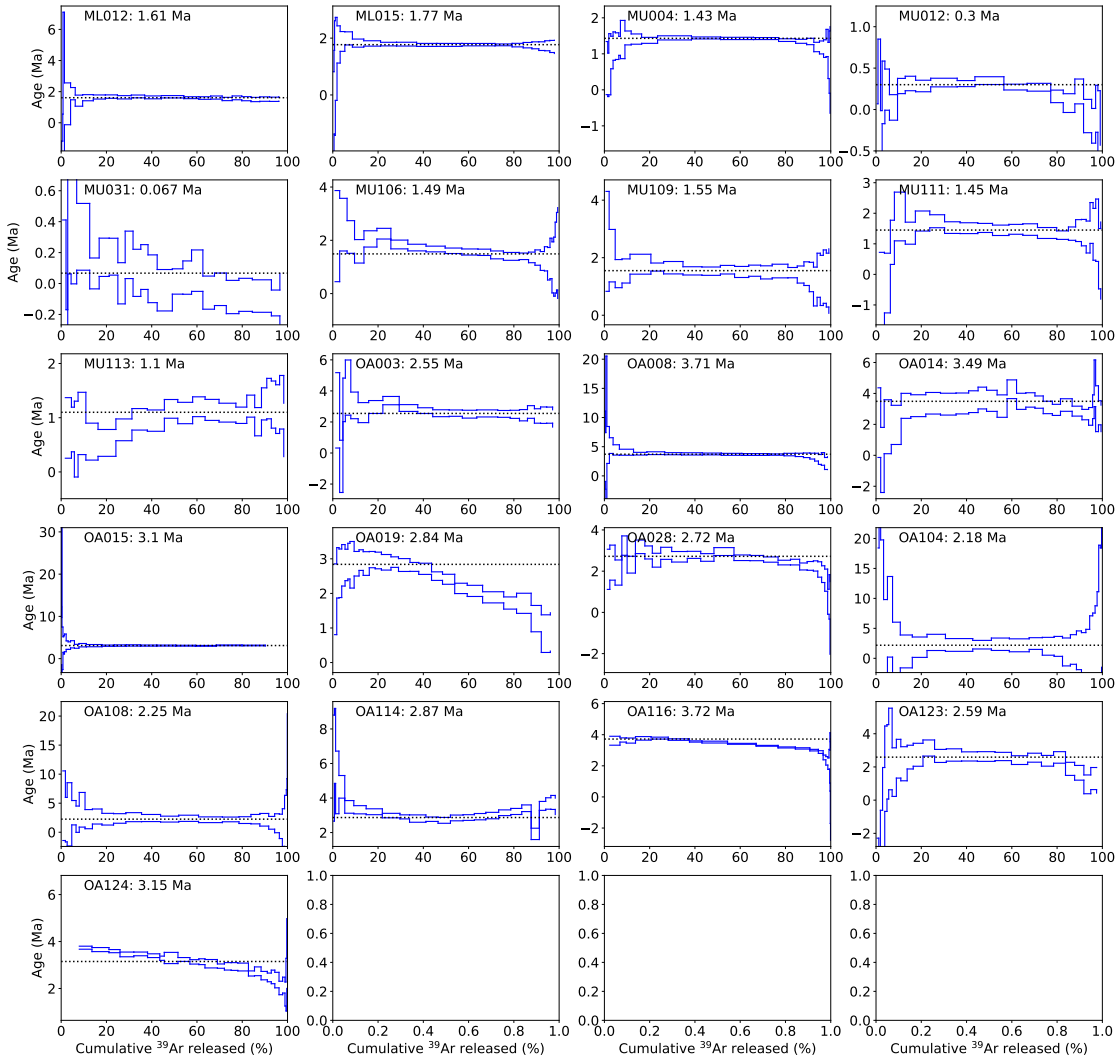

Fig. S1. Plots of Age against cumulative Argon released for age plateau and mini-plateau (OA019, OA116, OA124) age experiments. The mini-plateau ages for OA124 are concordant with total fusion ages from other samples from same site, and the mini-plateau age for OA019 is close to the age for OA028, a nearby lava flow which it is stratgraphically below.

Brendan Cych[a], Lisa Tauxe[a], Geoff Cromwell[b], John Sinton[c], and Anthony A.P. Koppers[d]

Table S1. Results analyzed using BiCEP from Antarctica (1) (sites with the prefix 'mc') and Northern Israel (2) (sites with the prefix 'GHI')

Site	Latitude	Longitude	Age (Ma)	Age 2σ	B_{min}	B_{median}	B_{max}
mc1001	-77.850000	166.640000	1.1800	0.0100	12.7	18.6	24.9
mc1002	-77.850000	166.690000	0.3300	0.0200	22.3	29.1	36.3
mc1009	-77.550000	166.200000	0.0740	0.0150	23.9	28.0	35.1
mc1015	-77.470000	169.230000	1.3300	0.0200	22.7	26.7	30.6
mc1020	-77.880000	165.020000	0.7700	0.0320	55.6	62.3	69.3
mc1029	-78.310000	164.800000	0.1800	0.0800	41.7	44.7	48.0
mc1031	-78.350000	164.300000	0.1330	0.0117	23.5	31.2	39.0
mc1032	-78.360000	164.300000	0.0078	0.0120	27.9	31.2	34.9
mc1036	-78.390000	164.270000	0.1200	0.0400	22.2	28.8	35.3
mc1103	-78.240000	163.360000	1.4210	0.0300	14.5	20.1	27.7
mc1109	-78.280000	163.540000	1.2610	0.0400	29.5	33.2	37.0
mc1111	-78.220000	162.790000	1.9900	0.0400	18.5	21.4	24.6
mc1115	-78.240000	162.960000	2.4600	0.3100	26.7	31.2	35.8
mc1119	-78.240000	162.960000	1.0800	0.2200	34.6	37.7	40.9
mc1120	-78.240000	163.090000	1.7560	0.0500	22.4	24.7	27.0
mc1121	-78.240000	162.950000	2.5050	0.0600	28.8	32.8	35.7
mc1127	-78.250000	163.730000	1.9420	0.0680	33.7	37.0	40.4
mc1135	-78.230000	166.560000	3.6000	0.0100	29.4	31.7	33.9
mc1139	-78.260000	163.080000	0.8820	0.0800	24.6	27.8	31.0
mc1140	-78.280000	163.000000	2.0430	0.0900	28.4	34.2	39.1
mc1145	-78.240000	162.893000	1.9000	0.1200	3.3	7.0	10.2
mc1147	-78.200000	162.960000	1.6300	0.3200	16.5	22.4	27.2
mc1155	-77.700000	162.250000	1.5000	0.0500	23.3	30.8	38.3
mc1157	-77.700000	162.260000	1.7100	0.0100	31.4	37.9	44.9
mc1160	-77.690000	162.350000	3.4700	0.0500	18.1	24.9	31.4
mc1165	-77.510000	169.330000	1.4510	0.0600	20.6	27.8	35.1
mc1167	-77.490000	169.290000	1.3800	0.1000	38.9	43.5	48.4
mc1200	-77.550000	166.160000	0.0730	0.0100	21.2	26.6	31.8
mc1302	-78.190000	165.320000	0.0400	0.0200	23.7	28.9	34.3
mc1304	-78.240000	163.360000	0.2900	0.0400	18.8	24.7	29.5
mc1305	-78.240000	163.230000	0.9000	0.2000	30.6	34.4	38.2
mc1306	-77.700000	162.690000	2.5600	0.2600	4.5	6.9	9.5
mc1307	-77.850000	166.670000	1.3300	0.2400	39.7	46.1	53.5
GHI01	33.126350	35.782270	0.1177	0.0358	20.1	25.2	30.2
GHI02	33.158050	35.776730	0.1296	0.0012	20.5	24.5	27.9
GHI03B	33.122790	35.724160	0.8420	0.0233	66.7	69.3	72.2
GHI03C	33.122790	35.724160	0.8420	0.0233	36.8	45.2	52.5
GHI03D	33.122790	35.724160	0.8420	0.0233	47.0	59.2	70.1
GHI05	32.960510	35.862240	0.1679	0.0255	19.7	22.6	25.0
GHI06	33.069580	35.771430	0.1145	0.0085	26.4	27.4	28.5
GHI07	33.085810	35.755890	0.6805	0.0183	33.6	40.9	47.7
GHI07C	33.085810	35.755890	0.6805	0.0183	21.0	23.2	25.2
GHI10	33.051680	35.849680	0.6149	0.0349	18.1	19.8	21.5
GHI18	33.025833	35.494912	1.6700	0.0400	30.9	37.3	43.6
GHI19	32.995278	35.525986	2.4500	0.0226	27.1	32.8	39.4
GHI20	32.926290	35.849940	1.6500	0.0200	29.9	31.8	33.5
GHI21	32.926290	35.849940	1.6765	0.0302	21.7	23.6	25.6
GHI25	33.218726	35.777062	0.8723	0.0053	44.7	52.9	60.8
GHI26	33.220000	35.776833	0.8704	0.0169	46.2	50.0	53.7
GHI27	33.212500	35.786157	1.1498	0.0348	33.5	36.9	40.6
GHI28	33.212500	35.786157	1.1912	0.0152	21.5	28.0	33.7
GHI29	33.179444	35.793218	0.7496	0.0945	28.7	31.1	33.2
GHI39	33.141000	35.682000	0.8476	0.1165	5.9	14.8	21.7
GHI40	33.141000	35.682000	0.7736	0.1949	4.7	7.1	9.8
GHI41	33.141000	35.683000	0.7902	0.0058	4.7	7.1	10.0
GHI44	33.042000	35.836000	1.4369	0.0195	45.6	48.9	52.6
GHI46	32.868290	35.829050	2.7442	0.0475	51.2	61.2	75.4

References

1. H Asefaw, L Tauxe, AAP Koppers, H Staudigel, Four-Dimensional Paleomagnetic Dataset: Plio-Pleistocene Paleodirection and Paleointensity Results From the Erebus Volcanic Province, Antarctica. *J. Geophys. Res. Solid Earth* **126**, e2020JB020834 (2021).
2. L Tauxe, H Asefaw, N Behar, AAP Koppers, R Shaar, Paleointensity Estimates from the Pleistocene of Northern Israel: Implications for hemispheric asymmetry in the time-averaged field. *Geochem. Geophys. Geosyst.* **n/a**, e2022GC010473 (2022).